Slat Noise Control Using a Slat Gap Filler

Yang Zhang*, Ross Richardson†, and Louis N. Cattafesta III‡
Florida Center for Advanced Aero-Propulsion (FCAAP), Florida A&M University and Florida State University, Tallahassee, Florida, 32310

Kyle A. Pascioni§, Meelan M. Choudhari¶, David P. Lockard‖, Mehdi R. Khorrami**, and Travis L. Turner††
NASA Langley Research Center, Hampton, VA, 23681

The leading edge slat of a high-lift system is one of the main noise contributors on many commercial aircraft during approach. This paper continues our previous studies on the gap filler for passive noise control on the 30P30N high-lift airfoil. An improved implementation of the gap filler was applied to minimize the effects of flow leakage encountered in the previous work, which resulted in spurious noise content in the far-field acoustic spectra. To evaluate the effect of passive flow control on the acoustics generated by the unsteady flow field, anechoic wind tunnel experiments are conducted on the two-dimensional, three-element high-lift airfoil with a gap filler mounted to the slat. The slat geometry modification associated with the gap filler alters the flow field in the cove region that dominates the generation of the acoustic field. A single angle of attack ($\alpha_k = 8°$) and three flow speeds corresponding to Reynolds numbers of $Re_c = 1.2e6$, $1.5e6$, and $1.71e6$ are selected as the test conditions. Steady surface pressure measurements are conducted to assess the effect of the treatments on the overall lift. Acoustic array measurements are used to evaluate the influence of the gap filler on the radiated noise. Delay and Sum beamforming is applied to locate the noise sources on the model and to provide the integrated spectra. The gap filler is found to eliminate the narrowband peaks in the acoustic spectra and, also, to yield a 10 dB reduction in the broadband noise in comparison with the baseline case. Time-resolved Particle Image Velocimetry results show that the flow features are significantly altered with the presence of the gap filler, which leads to a more stable slat cove shear layer and, thus, to weaker pressure and velocity fluctuations.

I. Nomenclature

C_l	=	lift coefficient
C_p	=	pressure coefficient
c	=	chord length
f	=	frequency
Re_c	=	chord-based Reynolds number
St_s	=	slat chord based Strouhal number
s	=	slat chord length
U_∞	=	freestream flow speed
u	=	streamwise velocity-component
v	=	vertical velocity-component
x	=	streamwise direction
y	=	vertical direction
z	=	spanwise direction

*Research faculty, Department of Mechanical Engineering, AIAA Member. yz12b@my.fsu.edu
†Graduate research assistant, Department of Mechanical Engineering, AIAA Student Member.
‡Professor and University Eminent Scholar, Department of Mechanical Engineering, AIAA Associate Fellow.
§Research Aerospace Engineer, AIAA member.
¶Aerospace Technologist, AIAA Fellow.
‖Aerospace Technologist, AIAA Associate Fellow.
**Aerospace Technologist, AIAA Associate Fellow.
††Aerospace Technologist, AIAA Associate Fellow.

α_k = angle of attack with Kevlar wall
ω_z = spanwise vorticity

II. Introduction

During the landing phase, deployed high-lift devices and the landing gear contribute a significant portion of the total aircraft noise. Along with the trailing edge flaps, the leading edge slat is often the dominant contributor to the noise associated with the high-lift devices [1]. Slat noise generation mechanisms are complicated and have been studied for many years. Slat noise usually contains both broadband and narrowband characteristics, which represent the combined outcome of several flow-induced source mechanisms. Khorrami et al. [2] and Singer et al. [3] showed that the high frequency tonal noise ($20 < St_s < 40$, where the characteristic length scale is the slat chord) is caused by vortex shedding from the blunt trailing edge of the deployed slat. Khorrami et al. [4] and Choudhari et al. [5] found the interaction of the slat shear layer with the high-lift geometry to be responsible for the low-to-mid frequency broadband component. It is well accepted that the strong narrowband peaks in the mid-Strouhal range ($1 < St_s < 5$) in both the near field surface pressure spectra and the far-field acoustic spectra are linked to a flow-acoustic feedback of slat-cove shear layer instabilities [6, 7]. The generation of these peaks is analogous to the Rossiter modes [8] in the context of open cavity flows. Also, recent phase-locked PIV measurements suggest the presence of a bulk cove oscillation at a low Strouhal number ($St_s \approx 0.15$), which is related to the unsteady impingement location, i.e., slat-cove shear layer flapping [9]. Slat noise is also known to have a broadband component with a peak in the Strouhal range close to unity. Choudhari and Khorrami [10] attributed this to the surface impingement of the unsteady vortical structures convected along the slat cove shear layer; this mechanism has been corroborated by Knacke and Thiele [11] using statistical correlation techniques.

With the knowledge of the noise generation mechanisms, a number of studies have been performed to reduce the flow unsteadiness and/or weaken its interaction with the airfoil surfaces in order to suppress the noise radiation. The passive approaches can be grouped into three categories:

1) Modifying the slat cusp with serrations or an extension to reduce the disturbances in the shear layer [12–16]. This concept generally reduces the growth and/or spanwise coherence of shear layer disturbances.
2) Filling the entire slat cove with a streamlined profile to minimize the flow separation [16–20]. With a streamlined geometry, the strong narrowband peaks induced by the shear layer disturbances no longer exist.
3) Reducing or sealing the gap between the slat and the main wing [16, 21–24]. This technique reduces the vortex shedding from the slat trailing edge and alters the reattachment point of the slat-cove shear layer.

The key requirement for an effective passive device is to significantly reduce the noise level (both broadband and narrowband) with minimal negative effects on the aerodynamics. Last but not the least, the passive device should be simple, without adding too much additional weight or mechanical complexity to the wing or any obstructions to the retraction of the slat.

The current study continues our previous investigation [16] of passive noise reduction concepts for the slat. The earlier study evaluated the effectiveness of slat cusp extensions and the cove filler, as well as investigating a preliminary implementation of a gap filler treatment. Although the previous gap filler implementation eliminated the narrowband peaks introduced by the flow instabilities along the slat-cove shear layer, it also introduced spurious high level humps and some additional peaks in the far-field acoustic spectra. Flow leakage through the gap filler was believed to be responsible for the spurious features of the measured noise signature. To help eliminate those undesirable features and, hence, to characterize the true effectiveness of the gap filler design, we applied an improved implementation of the gap filler that was designed to minimize the effects of the flow leakage encountered during the previous work. Both near-field surface pressures and the radiated far-field acoustics were measured to enable an improved assessment of the effects of the gap filler. Time-resolved Particle Image Velocimetry (TR-PIV) was also performed to investigate the changes in the underlying flow behavior.

III. Experimental Setup

A. Wind tunnel facility and airfoil model

The experiments were conducted in the Florida State Aeroacoustic Tunnel (FSAT) facility located at the Florida Center for Advanced Aero-Propulsion (FCAAP) at the Florida State University (FSU) [25]. All of the tests in the current work except for the TR-PIV were carried out in the test section with two Kevlar side panels. The schematic

and the main dimensions of the two-dimensional airfoil model are provided in Figure 1 and Table 1, respectively. The test section dimensions in the streamwise, spanwise, and vertical directions correspond to L=2.74 m, W=1.22 m, and H=0.91 m, respectively. The airfoil model has been used extensively to provide validation data for the AIAA workshop series on Benchmark Problems for Airframe Noise Computations (BANC). An overview of this workshop series was given by Refs. [26] and [27] provides a description of the 30P30N slat noise configuration as well as a summary of the computational and experimental contributions from the BANC-III Workshop. The model is mounted vertically in the middle of the FSAT test section, spanning the full tunnel height at this location. To minimize any blockage effects due to the model, the static pressure is measured from a tap on the contraction floor farther upstream, and a correction is applied based on the area ratio. Combinations of a single angle of attack (α_k = 8°) and three flow speeds (with chord-based Reynolds numbers of 1.2e6, 1.5e6, and 1.71e6) are selected as the test conditions in the current study. The geometric angle of attack equal to 8° produces a steady C_p distribution on the airfoil centerline that is similar to the free-air (i.e., an infinite freestream) numerical simulations based on the Shear Stress Transport (SST) turbulence model at 5.5° angle of attack [28]. Figure 1 shows two coordinate systems, in both of which x represents the streamwise direction, y is normal to the airfoil chord line, and z is along the airfoil span to make a right-handed system. The red coordinate system is used for PIV plots with its origin at the leading edge of the stowed airfoil; the blue coordinate system is used for Delay-and-Sum (DAS) source maps with the origin at the middle of the test section.

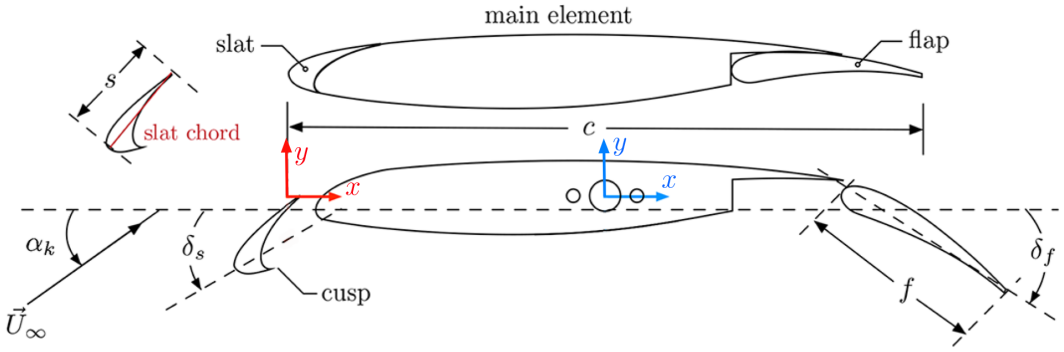

Fig. 1 Schematic of the 30P30N multi-element airfoil.

Table 1 Primary dimensions of 30P30N airfoil.

Stowed chord	c	0.457 m
Span length	b	0.914 m
Slat chord	s	0.15c
Flap chord	f	0.3c
Slat deflection angle	δ_s	30°
Flap deflection angle	δ_f	30°

A stainless steel gap filler is designed to alter the flow field near the slat. Using the streamlined gap filler, the vortex shedding from the trailing edge of the slat may be reduced or even eliminated. In addition, the flow path is blocked by the gap filler such that it can also alter the trajectory and reattachment of the shear layer, and minimize interaction of turbulent structures with the slat trailing edge. In a precursor to the current set of experiments, the tail of the gap filler was not bonded to the main wing, which resulted in an imperfect seal between these two elements (Figure 2(a)) [16] and is suspected to have caused a leakage of the flow at the point where the gap filler rests upon the main wing. In the current design, additional corner filler segments made of aluminum were made by using electrical discharge machining (Figure 2(b)). The corner fillers were sealed to the wing via silicone and an O-ring to prevent any leakage.

(a) Old version **(b) New version**

Fig. 2 Two versions of gap filler installation.

B. Steady surface pressure

To help characterize the aerodynamic performance of the airfoil with and without the gap filler, the mean surface pressure on the high-lift configuration was measured at a total of 122 static pressure ports that are instrumented on the 30P30N model. These ports are distributed both chordwise and across the span at selected locations as shown in Figure 3. Pressure scanners (Scanivalve DSA 3217) with multiple pressure ranges were used to acquire a total of 100 samples for each test condition at a sampling rate of 2 Hz. The 100 samples at each port were averaged to produce the steady pressure values. The coefficient of pressure is determined as $C_p = (p - p_\infty)/q_\infty$.

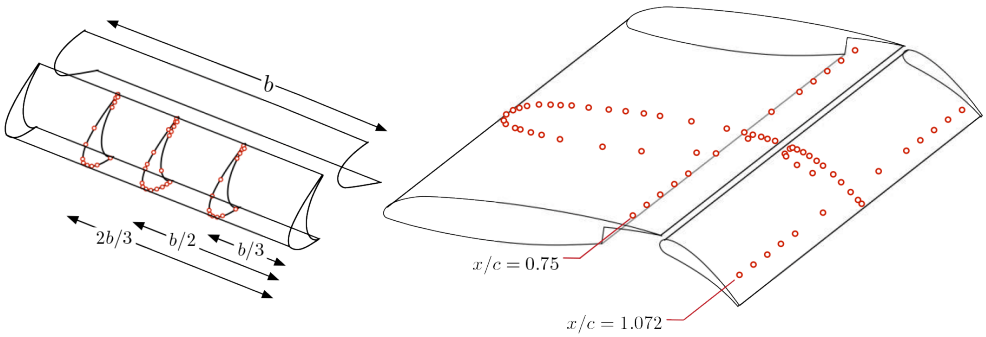

Fig. 3 Location of steady pressure taps on the 30P30N airfoil surface [7].

C. Far-field acoustic measurement

A phased microphone array comprised of a combination of 55 1/4-inch G.R.A.S. 40BE and Brüel and Kjær 4958 free field microphones was used to measure the far-field acoustic signals that were used to allow source localization via beamforming. The microphone layout was optimized via numerical simulations of the Point Spread Function (PSF) [29], and it has a log-spiral pattern as shown in Figure 4. The frame that holds the microphones is designed to minimize acoustic reflections. It is an aluminum skeleton frame that was fabricated via a waterjet cutting process and it is covered by 76 mm foam wedges, not shown. Each microphone is held away from the aluminum frame by a 0.15 m long steel rod in order to minimize any acoustic reflections and the near field scattering effects [7].

The microphone array is located at a distance of 1.18 m from the surface of the airfoil at $\alpha_k = 0^\circ$ and is centered on the axis of rotation of the airfoil at $x = 0.5c$ with respect to the stowed leading edge as shown in Figure 5. The microphone array faces the pressure side of the airfoil in order to measure the radiated sound in a flyover configuration. During the measurements, the Pitot probe located 0.9 m upstream is traversed out of the test section to avoid corrupting the acoustic data. The microphone data are simultaneously sampled at 204.8 kHz over a duration of 60 seconds by using multiple NI 4462 (24-bit) cards installed in the PXI 1045 chassis. Prior to the measurements, the sensitivity of each microphone was calibrated against a Brüel and Kjær pistonphone (Type 4220) at 250 Hz [7]. An acoustic correction due to the transmission through the Kevlar wall is also applied [7]. The DAS beamforming is applied to visualize the noise

source map as described in [7]. The spatial resolution is poor at low frequencies (< 1 kHz), with the 3-dB beamwidth being greater than 0.6 m. As the frequency is increased, the resolution is improved, but the number of potential false sources also increases due to more sidelobes [7].

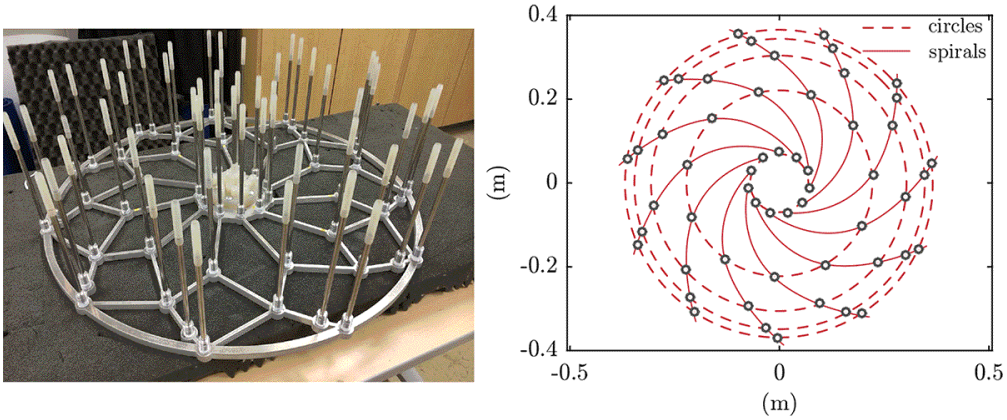

Fig. 4 Microphone array skeletal frame (left) and layout showing design criteria (right) [7].

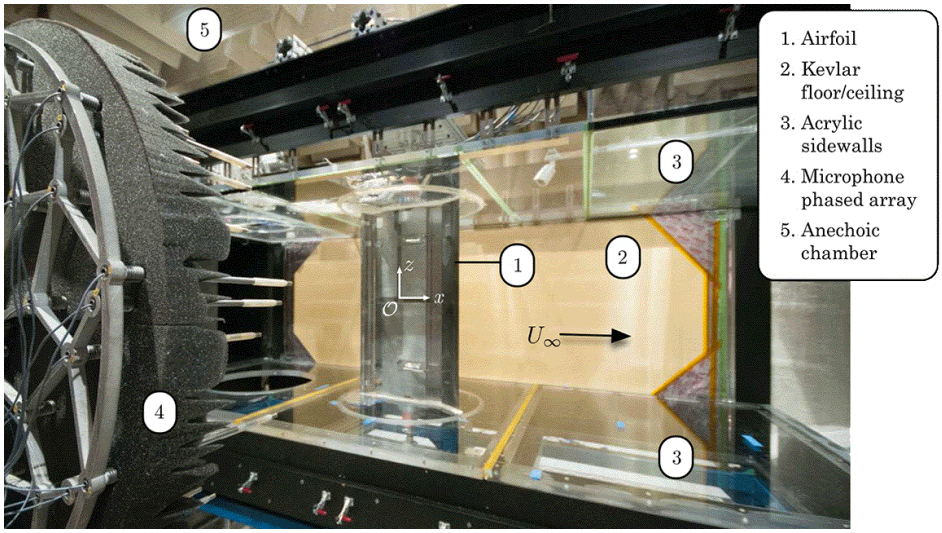

Fig. 5 Image of far-field acoustic measurement setup [7]. The Kevlar wall between the airfoil and the acoustic array is not shown in the picture.

D. High-speed Stereo Particle Image Velocimetry

In order to resolve the dynamics of the flow features in the vicinity of the slat, high-speed stereo PIV measurements have been performed (Figure 6). To that end, the Kevlar side panels used during the acoustic measurements were replaced with glass walls in order to allow optical access for the PIV measurements. The change in boundary conditions from the permeable Kevlar walls to the solid glass walls has an impact on the aerodynamics of the model, and specifically, on the effective angle of attack. To match the C_p distribution obtained at $\alpha_k = 8°$ with the Kevlar panels, the geometric angle of attack of the model was reduced to 5.5°. The laser beams generated by a Photonics DM dual-head laser pass through a series of optics before forming a laser sheet with a thickness of approximately 1.6 mm. Two Phantom V2012 high-speed cameras equipped with 180 mm Tamron SP Di Macro lenses, Scheimpflug adapters, and 532 nm band-pass filters were used for image acquisition. In addition, one camera has a 1.4× teleconverter installed and the other one has a 41.5 mm spacer, providing a closely matched magnification of the field of view. A fluorescent orange 3M tape is applied on the model surface to reduce the laser reflections. Tracing particles are introduced at the inlet of the wind

tunnel by a TSI 9307-6 seed particle generator using olive oil. Calibration is performed by using a LaVision Type 106-10 calibration plate, which is followed by a self-calibration procedure to correct for potential misalignment between the laser sheet and image plane. The sampling rate is 11 kHz in the double-frame acquisition mode with a full image resolution of 1280×464 pixels. This frame rate is sufficient to resolve the shedding of vortical flow structures by the slat cove shear layer. An attempt was also made to simultaneously capture the trailing edge region on the suction side. However, the laser energy degraded too much to illuminate the particles after passing through a beam splitter. Furthermore, the dynamics of the vortex shedding from the trailing edge was beyond the temporal resolution of our hardware. Thus, in the current study, we focused only upon the flow region in the vicinity of the slat cove, and the flow features within that region may be considered to be time-resolved (TR) by the stereo-PIV measurements, which are referred to as TR-PIV herein.

The TR-PIV images are acquired over a time interval of two seconds. Because a gradual degradation of the laser energy is observed in the time series of those images, we subtract the background signal based on a sliding average of 49 snapshots to enhance the contrast of particles. Geometric and algorithmic mask functions are used to mask out the no and low seeding regions, respectively. A 128×128 to 24×24 multi-pass scheme with a 75% overlap is used to calculate the velocity fields. Universal outlier detection is used to filter the spatially spurious outliers during the post-processing phase. This results in a vector resolution of approximately 2.2 vectors/mm (150 vectors/slat chord). The multi-variate outlier detection [30] is applied in MATLAB to remove statistically spurious data.

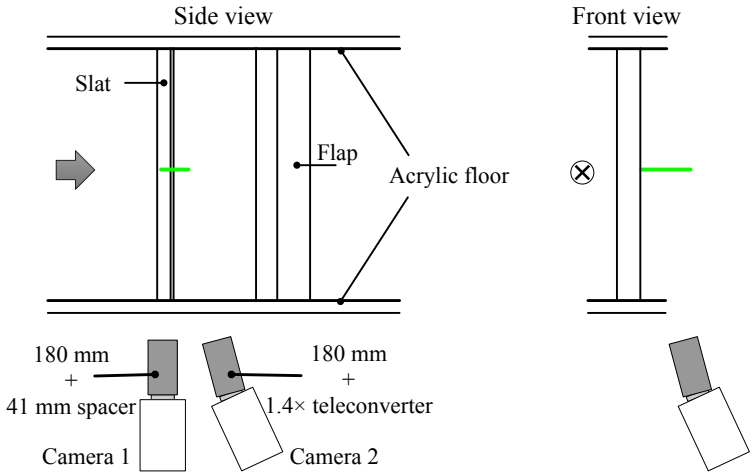

Fig. 6 Schematic of PIV setup (not to scale).

IV. Results and discussion

A. Steady surface pressure distribution

The chordwise C_p distribution along the midspan location for the gap filler case is compared with that in the baseline case in Figure 7. We note that some of the pressure taps are covered by the gap filler, and therefore, the pressures at these ports are not plotted. Similar to the results in the previous study [16], the gap filler has a significant influence on the C_p distributions within the slat region. Specifically, the gap filler reduces the pressure on the suction side and increases the pressure on the pressure side of the slat surface. The combined effect is likely to be an increased lift on the slat. At the leading edge of the main wing, pressure increases on the suction side, which leads to a reduction in the lift coefficient by approximately 0.25 at all Reynolds numbers used in the present tests as shown in Figure 8. We also observe that the C_p distribution over the flap is nearly unaffected by the introduction of the gap filler. These observations are quite consistent across the different Reynolds numbers. Given adequately dense C_p measurements, one can estimate the sectional lift coefficient C_l on individual elements of the high-lift configuration. Since some of the pressure taps along the slat pressure surface were covered by the gap filler, the C_p values at those locations are obtained from the baseline case in order to estimate the slat C_l in the presence of the gap filler. The velocity measurements shown in latter parts of this paper indicate relatively low velocities in the cove region in both of these cases; therefore, the

above approximation is expected to yield a fairly accurate estimate of the slat lift coefficient in the gap filler case. Based on this approximation, the gap filler leads to a higher C_l on the slat. While this additional lift does not compensate for the loss of lift from the main wing, we note that the lift generated on the gap filler (which, too, cannot be estimated from the experimental C_p measurements) should further offset the above loss in lift. Also, the design of the gap filler device was not optimized for the streamlined profile. With the current estimated total C_l and the reasons given above, it is possible that the gap filler would not cause any significantly adverse effects on the aerodynamics throughout the range of Reynolds number examined herein.

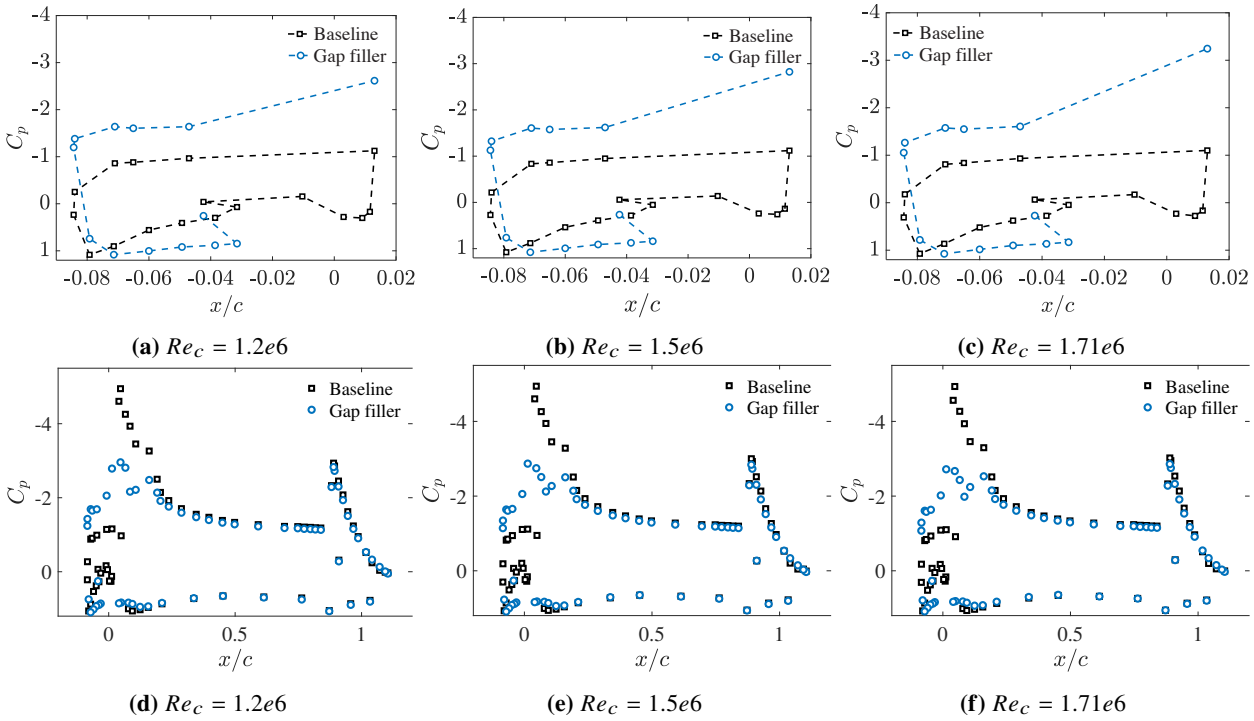

(a) Re_c = 1.2*e*6 **(b)** Re_c = 1.5*e*6 **(c)** Re_c = 1.71*e*6

(d) Re_c = 1.2*e*6 **(e)** Re_c = 1.5*e*6 **(f)** Re_c = 1.71*e*6

Fig. 7 C_p distribution along the centerline with and without the gap filler installed. First row: slat; second row: total.

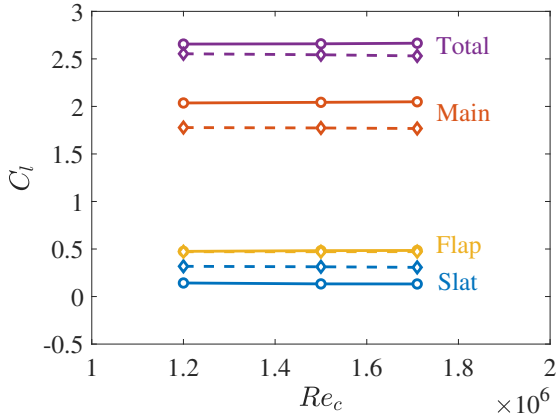

Fig. 8 C_l values for baseline and gap filler cases from static pressure measurements at the centerline pressure taps over a range of Reynolds numbers. Solid lines indicate the baseline case, and the dashed lines indicate the controlled case.

B. DAS beamforming and integrated spectra of far-field acoustics

In addition to the near-field steady pressure distribution, the far-field acoustic measurements are used to assess the noise radiation. For reference, the noise source maps are superimposed on the schematic of the wind tunnel as illustrated in Figure 9, where the flow is from left to right. The thin vertical lines between $x = -50$ cm and 50 cm indicate the boundaries of the slat, the main wing, and the flap at $\alpha_k = 8°$, as projected on the x-z plane. The boundaries of the vertical domain correspond to the top and bottom walls of the wind tunnel, and the full length of the test section is included in the figure. The DAS domain is set to be $x \in$[-1 m, 1 m] and $z \in$[-0.457 m, 0.457 m].

The DAS beamforming source maps in Figures 10 and 11 show the dominant noise sources obtained from the phased microphone array at two different Reynolds numbers. It is instructive to examine the source maps at the characteristic frequencies associated with the first three tonal peaks introduced by the shear layer shedding from the slat cusp in the baseline cases. For the baseline cases, the high noise regions are distributed along the span of the slat. A comparison of the noise source levels at the two flow speeds indicates that the noise introduced by the slat becomes more intense with increasing flow speed. The results at both Reynolds numbers show that the introduction of the gap filler leads to a downstream shift in the location of the highest noise levels in the beamforming maps. The dominant noise sources are now centered in the flap region, indicating that the slat cove region is no longer the primary source of noise and that the noise levels associated with that region have become substantially lower than the flap noise. This observation is consistent with the measurements obtained at the remaining Reynolds numbers.

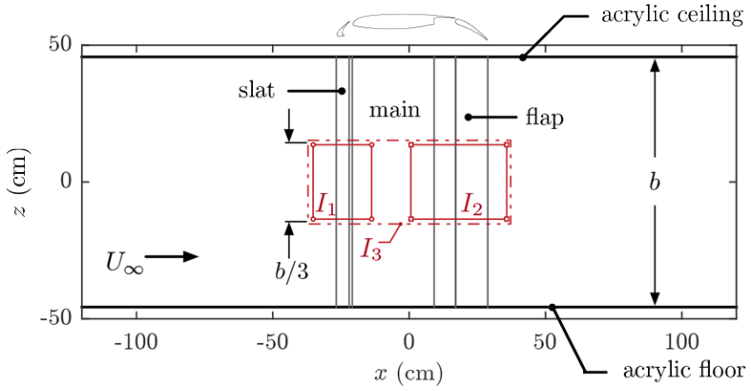

Fig. 9 Schematic of source map background and definition of integration regions [7].

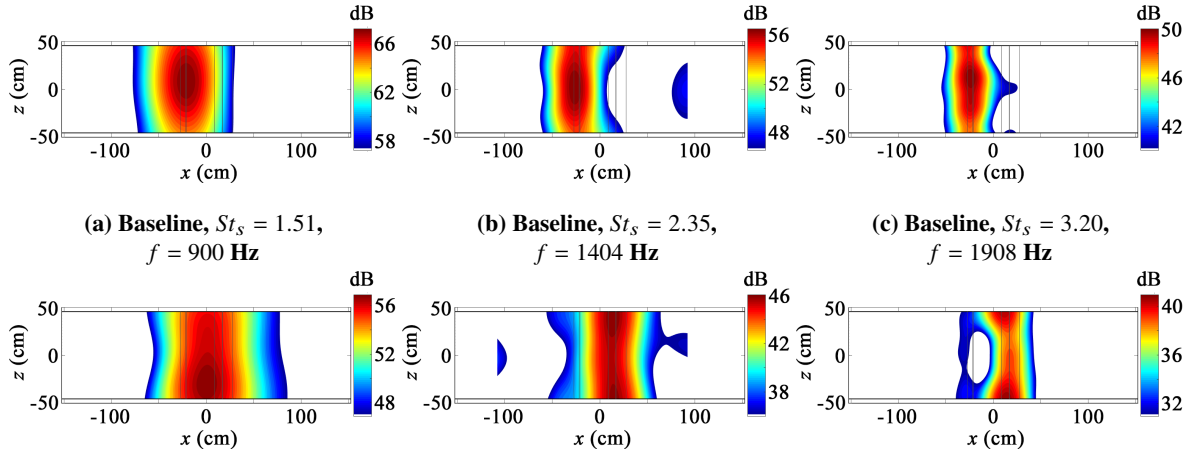

(a) Baseline, $St_s = 1.51$, $f = 900$ Hz **(b) Baseline, $St_s = 2.35$, $f = 1404$ Hz** **(c) Baseline, $St_s = 3.20$, $f = 1908$ Hz**

(d) Gap filler, $St_s = 1.51$, $f = 876$ Hz **(e) Gap filler, $St_s = 2.35$, $f = 1344$ Hz** **(f) Gap filler, $St_s = 3.20$, $f = 1776$ Hz**

Fig. 10 Source maps for $\alpha_k = 8°$ at $Re_c = 1.2 \times 10^6$ for narrowband DAS with 10 dB dynamic range relative to peak level. The center frequencies correspond to the first three shear layer modes introduced by the slat cusp.

The noise source levels are approximately uniform across the central one third of the airfoil span, and therefore, integrated DAS beamforming over the region I_1 as defined in Figure 9 are used to characterize the far-field acoustic spectra associated with the 2D high-lift configuration. The results are shown in Figure 12 and they provide a quantitative assessment of the effect of the gap filler on the radiated acoustic field. In the previous study [16], strange humps ($3 < St_s < 10$) with additional peaks ($St_s > 10$) had been observed in the measured spectra. With the improved design of the seal, these spurious features no longer exist in the integrated spectra. Similarly, the tonal peaks introduced by the instability waves in the slat cove shear layer have been eliminated, with a net reduction of greater than 10 dB for $1 < St_s < 5$. An additional reduction of approximately 10 dB in the broadband noise is also observed for $St_s > 2$. These results strongly suggest that the feedback loop inside the slat cove is disrupted by the installation of the gap filler.

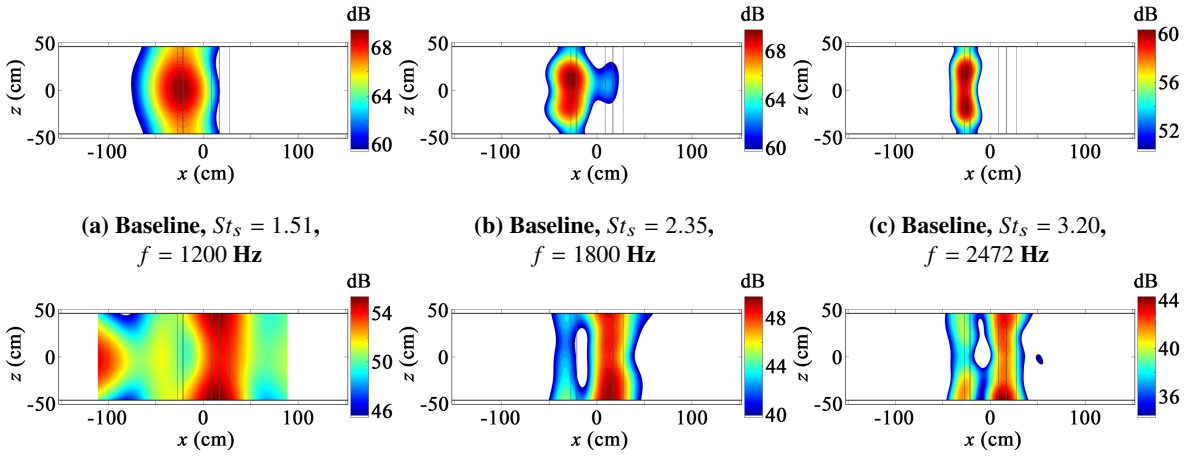

(a) Baseline, $St_s = 1.51$, $f = 1200$ Hz **(b) Baseline, $St_s = 2.35$, $f = 1800$ Hz** **(c) Baseline, $St_s = 3.20$, $f = 2472$ Hz**

(d) Gap filler, $St_s = 1.51$, $f = 1224$ Hz **(e) Gap filler, $St_s = 2.35$, $f = 1824$ Hz** **(f) Gap filler, $St_s = 3.20$, $f = 2496$ Hz**

Fig. 11 Source maps for $\alpha_k = 8°$ at $Re_c = 1.71 \times 10^6$ for narrowband DAS with 10 dB dynamic range relative to peak level. The center frequencies correspond to the first three shear layer modes introduced by the slat cusp.The flow direction is from left to right

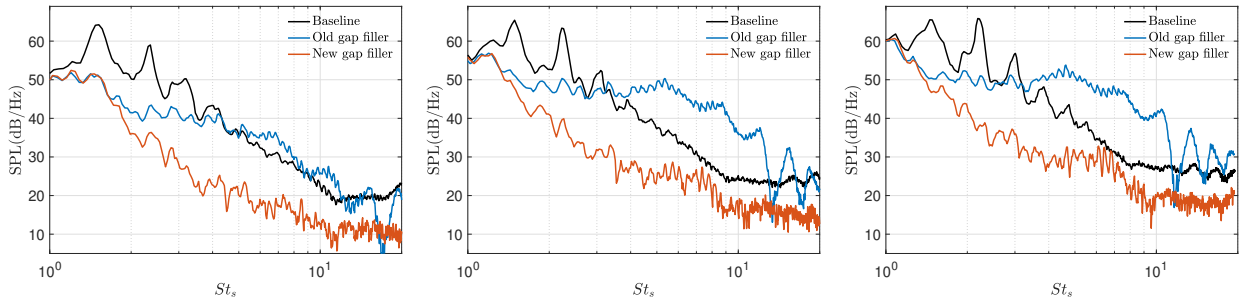

(a) $Re_c = 1.2 \times 10^6$ **(b)** $Re_c = 1.5 \times 10^6$ **(c)** $Re_c = 1.71 \times 10^6$

Fig. 12 Comparison of integrated sound pressure spectra between baseline, previous study, and current study using gap filler from region I_1 in the Kevlar test section. The sound pressure levels are scaled to a 1 m span at 1 m observer distance.

C. Velocity fields

Flow visualization based on the PIV can help elucidate some of the flow physics underlying the observed noise reduction during the far-field acoustic measurements. Due to the imperfections of flow seeding during the PIV experiments and the outliers in the processed vector fields, a random subset of vectors are missing from the field of view.

These missing vectors can lead to errors when calculating the spectra of the velocity components. Therefore, a POD based interpolation method, called GAPPY-POD [31], is applied to fill in the missing vectors. It should be noted that the coordinate system for the PIV results shown herein is fixed with respect to the airfoil position at 0° angle of attack. Therefore, even though the flow is from left to right, the x-direction is *not* the flow direction.

Figures 13(a) and 13(b) display the contours of the time-averaged velocity components u and v, respectively, for the baseline case. For ease of interpretation, the streamlines associated with the time averaged velocity field have been superimposed on both contour plots. Similar results for the gap filler case are shown in Figs. 13(c) and 13(d), respectively. The velocity field in the baseline case is essentially the same as the earlier set of results presented in [7]. Figures 13(c) and 13(d)) demonstrate the substantial alteration of the flow path due to the presence of the gap filler. With the blocking of the gap between the slat and main wing, the slat cove shear layer no longer reattaches to the slat pressure surface. Instead, the shear layer is relatively straight and reattaches much further downstream on the lower side of the main wing. Note that the shear layer reattachment point on the main wing is close to the original stagnation point. This results in an enlarged recirculation bubble enclosed by the shear layer. A secondary smaller recirculation region is also observed in the upper part of the recirculation region, i.e., underneath the gap filer.

The original reattachment point on the cove surface in the baseline case generates an acoustic source that radiates upstream propagating sound that further enhances the formation of shear layer disturbances near the cusp, analogous to the classical acoustic feedback loop in cavity flows. The resonances associated with this acoustic feedback loop result in several high level tonal peaks as observed in the far-field acoustic spectra. With the reattachment point shifted to the main wing, the original acoustic feedback loop is virtually eliminated. On the other hand, the vorticity of the shear layer is much weaker in the gap filler case (Figure 14(b)), indicating a less intense shear layer that decays before reattaching to the main wing. As a result, the far-field sound pressure levels, including both tonal and broadband, are significantly reduced as shown in Figure 12.

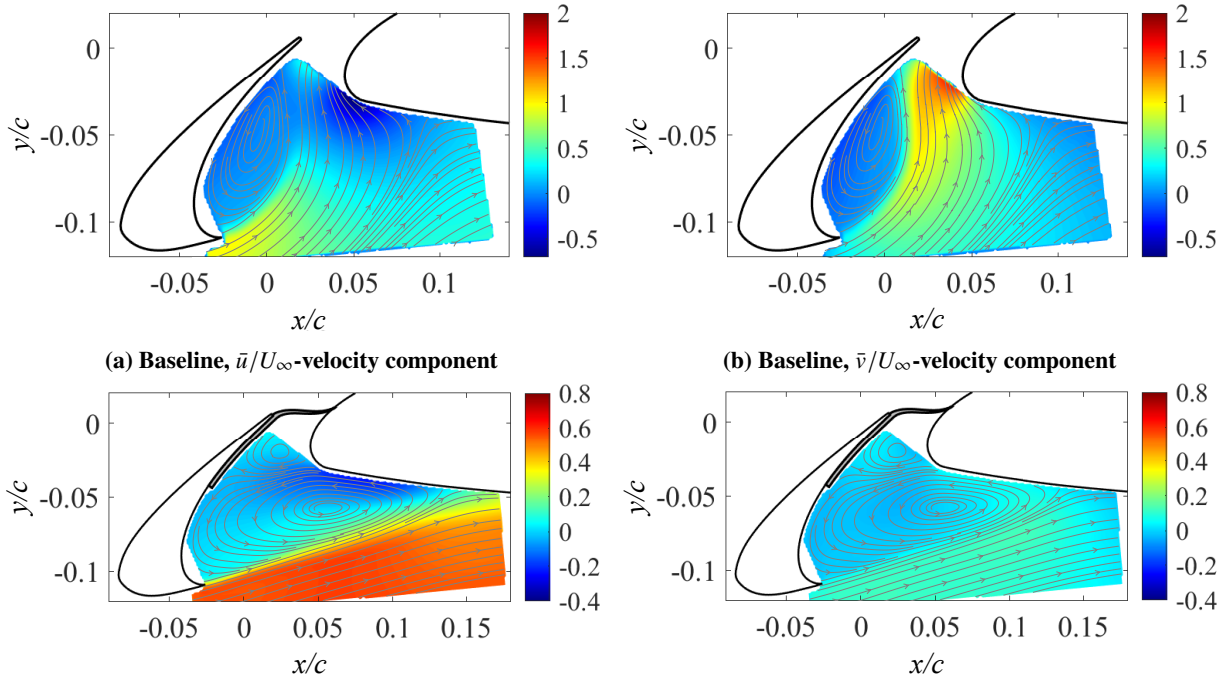

(a) Baseline, $\bar{u}/U_\infty$-velocity component

(b) Baseline, $\bar{v}/U_\infty$-velocity component

(c) Gap filler, $\bar{u}/U_\infty$-velocity component

(d) Gap filler, $\bar{v}/U_\infty$-velocity component

Fig. 13 Time-averaged velocity components of baseline and gap filler cases with streamlines superimposed.

The time-resolved flow fields are decomposed into spatial and temporal coherent structures using the spectral form of the proper orthogonal decomposition (SPOD) technique [32]. The SPOD based spectra of the ω_z vorticity modes for the baseline and gap filler configurations are shown in Figures 15(a) and 15(b), respectively. The spectra for the baseline case indicate several tonal peaks that are consistent with the frequencies of the spectral peaks in far-field acoustic measurements for that case. With the gap filler installed, there are no distinctive tonal peaks present in the ω_z spectra,

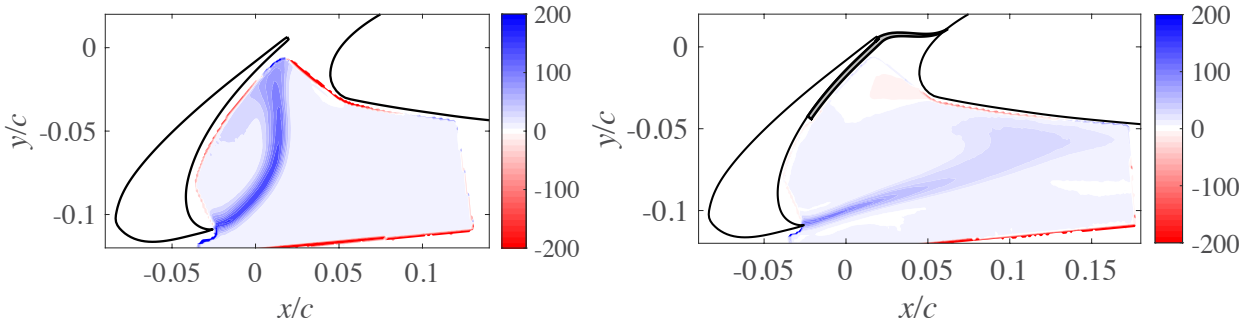

(a) Baseline **(b) Gap filler**

Fig. 14 Time-averaged spanwise voriticity $\omega_z c/U_\infty$ with and without gap filler installed

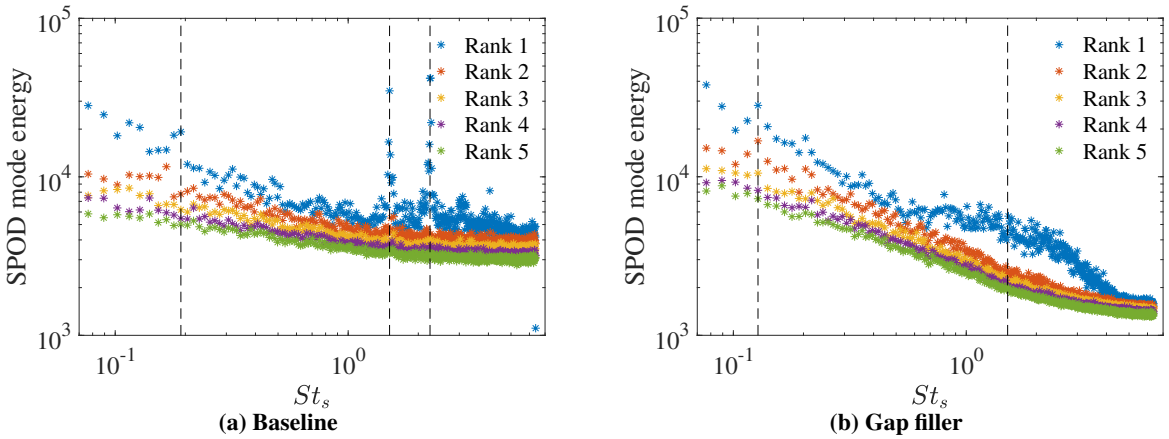

(a) Baseline **(b) Gap filler**

Fig. 15 Spectra of SPOD ω_z of first 5 highest rank modes. The mode shapes associated with the dashed-line frequencies are extracted.

other than a mild peak near $St_s = 0.13$. The absence of dominant spectral peaks at $St_s > 1$ is again consistent with the far-field acoustic spectra. Instead, a broadband hump shows up in the spectra for the gap filler case. Since there are no distinctive peaks within the hump, we picked the frequency at $St_s = 1.51$ (i.e., the same frequency as the dominant shear layer mode in the baseline case) to show the modal shape. A weighting function emphasizing a spatial proximity to the shear layer was also applied, but was found to have negligible effects on the mode spectra.

Next, we discuss the modes at the frequencies corresponding to the spectral peaks indicated by the dashed lines in Figure 15. In order to illustrate the dynamics of the SPOD modes, the three modes of spanwise vorticity, ω_z, are displayed in Figure 16 for four different phase angles with an interval of $\pi/2$ radians between each successive pair of images. The previous study by Pascioni and Cattafesta [9] related the bulk oscillation due to the shear layer flapping as the mechanism responsible for the peak in the baseline spectra at $St_s = 0.15$. The flow structures of the first mode are mainly located inside the cove recirculation bubble. The other two modes are seen to be the typical shear layer modes. The trajectory of the shear layer is clearly presented by the adjacent colored pairs. The flow structures increase in size along the shear layer and eventually impinge on the slat cove surface. The third mode is similar to the second mode, but with a shorter wavelength of the structures as the result of a higher oscillation frequency. For the gap filler case, the motion of large structures at $St_s = 0.13$ does not show up in the integrated SPL because the corresponding frequency of 110 Hz is below the chamber cut-off frequency of 250 Hz. The modal shape associated with the frequency ($St_s = 1.51$) at the middle of the hump frequency has the signature of a shear layer mode. By examining several modes of nearby frequencies from the hump, they all represent similar shear layer characteristics. Instead of locking in a single frequency of vortex shedding, this wide hump indicates that the shear layer experiences a broadband frequency modulation of the vortex shedding. In addition, the growing vortical structures decay before reaching the main wing, which results in a weaker reattachment unlike the intense impingement by large structures in the baseline case. These mechanisms lead to

a lower level of noise radiation in the gap filler case.

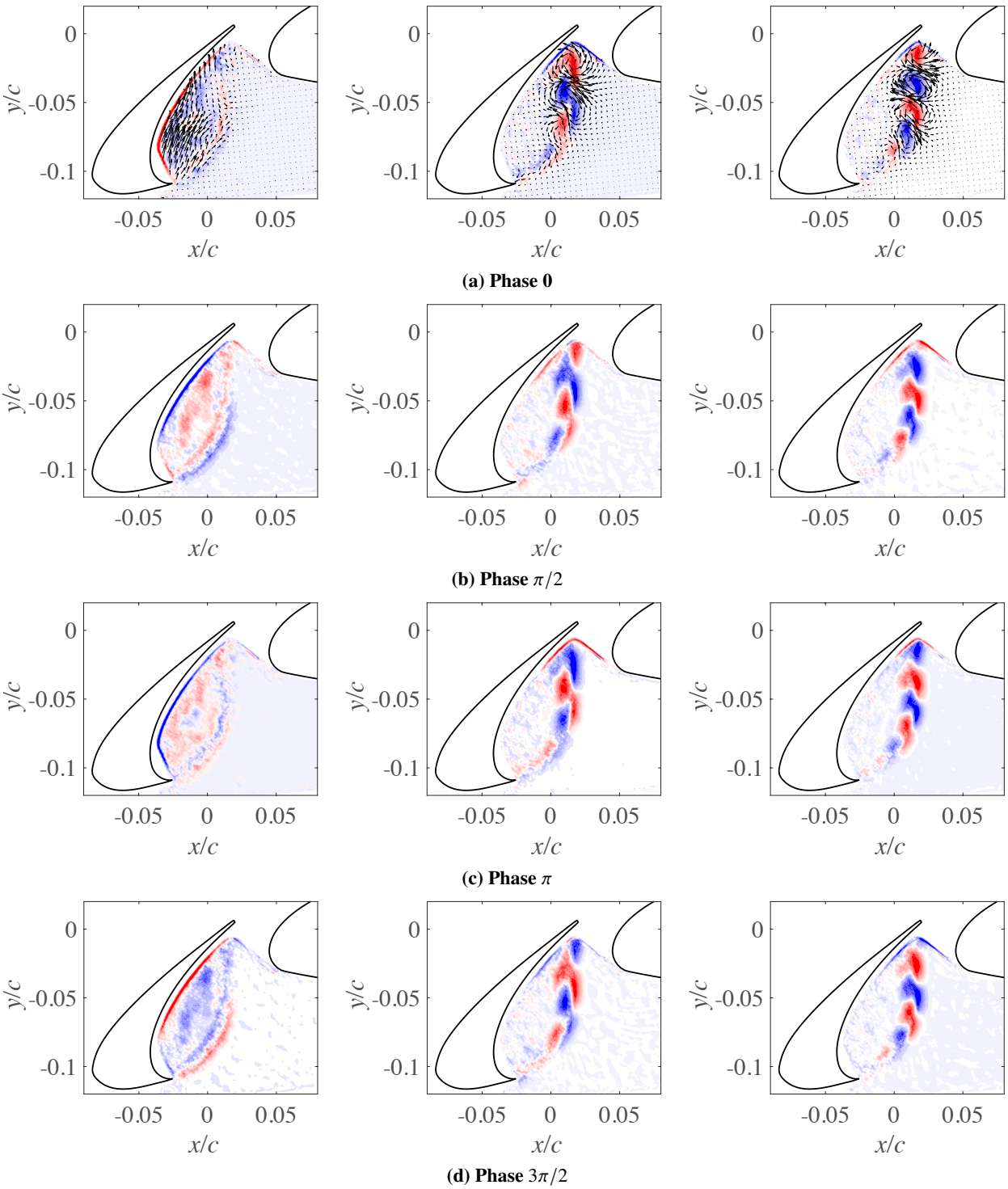

(a) Phase 0

(b) Phase $\pi/2$

(c) Phase π

(d) Phase $3\pi/2$

Fig. 16 Modal shapes at different phases for the baseline case. Velocity vectors are superimposed on the first phase. Left: $St_s = 0.19$**; middle:**$St_s = 1.51$**; right:** $St_s = 2.25$**.**

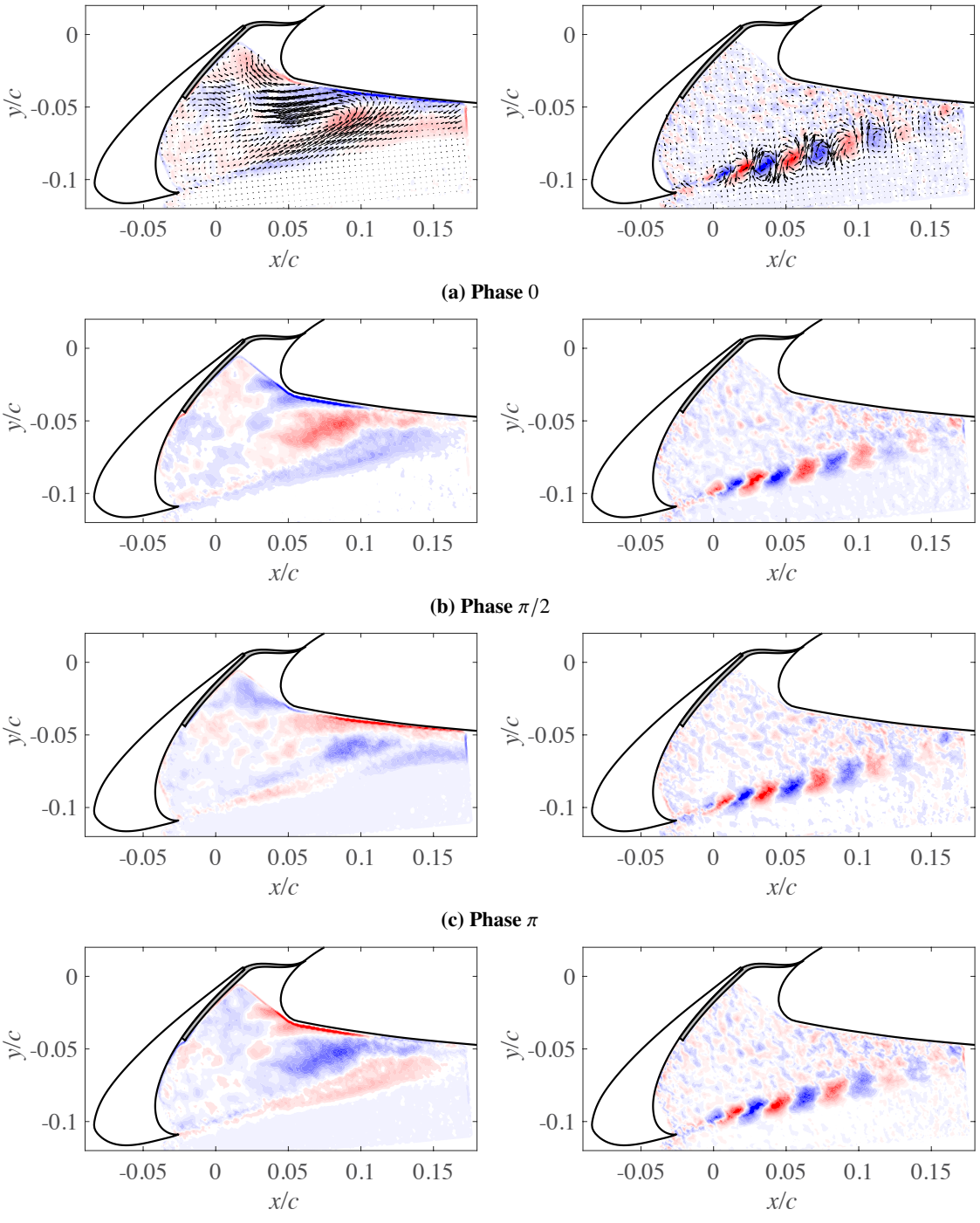

(a) Phase 0

(b) Phase $\pi/2$

(c) Phase π

(d) Phase $3\pi/2$

Fig. 17 Modal shapes at different phases for the gap filler case. Vectors are superimposed on the first phase. Left: $St_s = 0.13$**; right:** $St_s = 1.51$

V. Conclusions

The current research has continued our previous study [16] on passive control devices that reduce the slat noise from a high-lift airfoil system. An improved implementation of the gap filler has prevented the suspected flow leakage

experienced by the earlier version of the same device during previous tests. The new results have shown that the improved gap filler eliminates all of the tonal peaks due to the feedback loop involving the amplification of shear layer instability waves and, furthermore, it also reduces the broadband noise by approximately 10 dB for $St_s > 2$. The effects of the gap filler on the total lift could not be assessed due to the missing data inside the slat cove at this point. However, the TR-PIV measurements have shown that the gap filler changes the flow path significantly. In particular, the slat cove shear layer reattaches on the main wing instead of the pressure surface of the slat, resulting in an enlarged region of recirculation. The spectral, i.e., frequency domain, proper orthogonal decomposition (SPOD) analysis has revealed the flow structures underlying the low frequency bulk oscillation at $St_s = 0.15$ as well as those associated with two additional modes related to the instability of the slat-cove shear layer from the baseline slat. The flow in the presence of the gap filler is shown to be much "quieter" as no energetic peaks are observed in the SPOD spectra. This suppression of the near-field unsteadiness is achieved via the break up of the acoustic feedback loop through the altered shear layer trajectory due to the absence of the slat trailing edge and the slat gap. Although the resonant tones induced by the slat-cove shear layer may not always exist in larger scale tests [33], the gap filler concept should still serve as an effective device for passive noise control, and the data presented herein can be used for validation of related CFD simulations at the same Re_c.

Acknowledgments

This research was supported by NASA under contract 80NSSC18P3447. The authors gratefully acknowledge the NASA Langley, FCAAP and MagLab machine shops for the fabrication of the noise control treatments.

References

[1] Dobrzynski, W., "Almost 40 Years of Airframe Noise Research: What Did We Achieve?" *Journal of Aircraft*, Vol. 47, 2010, pp. 353–367.

[2] Khorrami, M. R., Berkman, M. E., and Choudhari, M., "Unsteady Flow Computations of a Slat with a Blunt Trailing Edge," *AIAA Journal*, Vol. 38, No. 11, 2000, pp. 2050–2058.

[3] Singer, B. A., Lockard, D. P., and Brentner, K. S., "Computational Aeroacoustic Analysis of Slat Trailing-Edge Flow," *AIAA Journal*, Vol. 38, No. 9, 2000, pp. 1558–1564.

[4] Khorrami, M. R., Singer, B. A., and Berkman, M. E., "Time-Accurate Simulations and Acoustic Analysis of Slat Free Shear Layer," *AIAA Journal*, Vol. 40, 2002, pp. 1284–1291. https://doi.org/10.2514/3.15195.

[5] Choudhari, M., Lockard, D., Macaraeg, M., Singer, B., Streett, C., Neubert, G., Stoker, R., Underbrink, J., Berkman, M., Khorrami, M., and Sadowski, S., "Aeroacoustic Experiments in the Langley Low-Turbulence Pressure Tunnel," Tech. rep., NASA, 2002. TM 2002-211432.

[6] Terracol, M., Manoha, E., and Lemoine, B., "Investigation of the Unsteady Flow and Noise Generation in a Slat Cove," *AIAA Journal*, Vol. 54, No. 2, 2016, pp. 469–489.

[7] Pascioni, K., "An Aeroacoustic Characterization of a Multi-Element High-Lift Airfoil," Ph.D. thesis, Florida State University, Tallahassee, FL, 2017.

[8] Rossiter, J. E., "Wind-tunnel Experiments on the Flow over Rectangular Cavities at Subsonic and Transonic Speeds," Tech. rep., Aeronautical Research Council Reports and Memoranda, 1964. No. 3438.

[9] Pascioni, K. A., and Cattafesta, L. N., "Unsteady Characteristics of a Slat-Cove Flow Field," *Phys. Rev. Fluids*, Vol. 3, 2018. https://doi.org/10.1103/PhysRevFluids.3.034607.

[10] Choudhari, M. M., and Khorrami, M. R., "Effect of Three-Dimensional Shear-Layer Structures on Slat Cove Unsteadiness," *AIAA Journal*, Vol. 45, No. 9, 2007, pp. 2174–2186.

[11] Knacke, T. J., and Thiele, F., "Numerical Analysis of Slat Noise Generation," *19th AIAA/CEAS Aeroacoustics Conference*, American Institute of Aeronautics and Astronautics, Reston, Virginia, 2013. AIAA paper 2013-2162.

[12] Dobrzynski, W., Gehlhar, B., and Buchholz, H., "Model and full scale high-lift wing wind tunnel experiments dedicated to airframe noise reduction," *Aerospace Science and Technology*, Vol. 5, No. 1, 2001, pp. 27–33. https://doi.org/10.1016/s1270-9638(00)01079-8.

[13] Bridges, J., and Brown, C. A., "Parametric Testing of Chevrons on Single Flow Hot Jets," 2004. AIAA Paper 2004-2824.

[14] Khorrami, M. R., and Lockard, D. P., "Effects of Geometric Details on Slat Noise Generation and Propagation," *International Journal of Aeroacoustics*, Vol. 9, No. 4-5, 2010, pp. 655–678. https://doi.org/10.1260/1475-472X.9.4-5.655.

[15] Kopiev, V., Zaitsev, M., Belyaev, I., and Mironov, M., "Noise Reduction Potential Through Slat Hook Serrations," 2011. AIAA Paper 2011-2909.

[16] Zhang, Y., O'Neill, A., Cattafesta, L. N., Pascioni, K., Choudhari, M., Khorrami, M. R., Lockard, D. P., and Turner, T., "Assessment of Noise Reduction Concepts for Leading-Edge Slat Noise," *2018 AIAA/CEAS Aeroacoustics Conference*, American Institute of Aeronautics and Astronautics, 2018. https://doi.org/10.2514/6.2018-3461.

[17] Horne, W., James, K., Arledge, T., Soderman, P., Burnside, N., and Jaeger, S., "Measurements of 26%-Scale 777 Airframe Noise in the NASA Ames 40- by 80 Foot Wind Tunnel," *11th AIAA/CEAS Aeroacoustics Conference*, American Institute of Aeronautics and Astronautics, 2005. https://doi.org/10.2514/6.2005-2810.

[18] Imamura, T., Ura, H., Yokokawa, Y., Enomoto, S., Yamamoto, K., and Hirai, T., "Designing of Slat Cove Filler as a Noise Reduction Device for Leading-edge Slat," *13th AIAA/CEAS Aeroacoustics Conference (28th AIAA Aeroacoustics Conference)*, American Institute of Aeronautics and Astronautics, 2007. https://doi.org/10.2514/6.2007-3473.

[19] Jawahar, H. K., Azarpeyvand, M., and Ilario, C., "Experimental Investigation of Flow Around Three-Element High-Lift Airfoil with Morphing Fillers," *23rd AIAA/CEAS Aeroacoustics Conference*, American Institute of Aeronautics and Astronautics, 2017. https://doi.org/10.2514/6.2017-3364.

[20] Arena, G., Groh, R., Pirrera, A., Scholten, W., Hartl, D., and Turner, T., "A Tailored Nonlinear Slat-Cove Filler for Airframe Noise Reduction," *Volume 1: Development and Characterization of Multifunctional Materials; Modeling, Simulation, and Control of Adaptive Systems; Integrated System Design and Implementation*, American Society of Mechanical Engineers, 2018. https://doi.org/10.1115/smasis2018-8079.

[21] Herr, M., Pott-Pollenske, M., Ewert, R., Boenke, D., Siebert, J., Delfs, J., Rudenko, A., Büscher, A., Friedel, H., and Mariotti, I., "Large-Scale Studies on Slat Noise Reduction," *21st AIAA/CEAS Aeroacoustics Conference*, American Institute of Aeronautics and Astronautics, 2015. https://doi.org/10.2514/6.2015-3140.

[22] Turner, T. L., and Long, D. L., "Development of a SMA-Based, Slat-Gap Filler for Airframe Noise Reduction," *23rd AIAA/AHS Adaptive Structures Conference*, American Institute of Aeronautics and Astronautics, Reston, Virginia, 2015. AIAA paper 2015-0730.

[23] Pagani, C. C., Souza, D. S., and Medeiros, M. A., "Experimental investigation on the effect of slat geometrical configurations on aerodynamic noise," *Journal of Sound and Vibration*, Vol. 394, 2017, pp. 256–279. https://doi.org/10.1016/j.jsv.2017.01.013.

[24] Lu, W., Liu, P., and Guo, H., "Experimental Study on Comparison on Noise Characteristics of Noise Reduction Leading-edge Slats," *25th AIAA/CEAS Aeroacoustics Conference*, American Institute of Aeronautics and Astronautics, 2019. https://doi.org/10.2514/6.2019-2404.

[25] Pascioni, K., Reger, R., Edstrand, A., and Cattafesta, L., "Characterization of an Aeroacoustic Wind Tunnel Facility," Vol. 249, 2014, pp. 3966–3975. 43rd International Congress on Noise Control Engineering.

[26] Choudhari, M. M., and Lockard, D. P., "Assessment of Slat Noise Predictions for 30P30N High-Lift Configuration from BANC-III Workshop," *21st AIAA/CEAS Aeroacoustics Conference*, American Institute of Aeronautics and Astronautics, Reston, Virginia, 2015. https://doi.org/doi:10.2514/6.2015-2844, aIAA Paper 2015-2844.

[27] Choudhari, M. M., and Lockard, D. P., "Simulation & Measurement of Airframe Noise: A BANC Workshops Perspective," *Progress and Challenges in Validation Testing for Computational Fluid Dynamics*, Zarazoga, Spain, 2016.

[28] Choudhari, M. M., Lockard, D. P., Khorrami, M. R., and Mineck, R. E., "Slat Noise Simulations: Status and Challenges," *Inter-Noise 2011*, Osaka, Japan, 2011.

[29] Reger, R., Zawodny, N., Pascioni, K., Wetzel, D., Liu, F., and Cattafesta, L., "Design-Optimization of a Broadband Phased Microphone Array for Aeroacoustic Applications," *Journal of the Acoustical Society of America*, Vol. 131, 2012.

[30] Griffin, J., Schultz, T., Holman, R., Ukeiley, L. S., and Cattafesta, L. N., "Application of multivariate outlier detection to fluid velocity measurements," *Experiments in Fluids*, Vol. 49, No. 1, 2010, pp. 305–317. https://doi.org/10.1007/s00348-010-0875-3.

[31] Saini, P., Arndt, C. M., and Steinberg, A. M., "Development and evaluation of gappy-POD as a data reconstruction technique for noisy PIV measurements in gas turbine combustors," *Experiments in Fluids*, Vol. 57, No. 7, 2016. https://doi.org/10.1007/s00348-016-2208-7.

[32] Towne, A., Schmidt, O. T., and Colonius, T., "Spectral proper orthogonal decomposition and its relationship to dynamic mode decomposition and resolvent analysis," *Journal of Fluid Mechanics*, Vol. 847, 2018, pp. 821–867. https://doi.org/10.1017/jfm.2018.283, URL https://doi.org/10.1017%2Fjfm.2018.283.

[33] Dobrzynski, W., Ewert, R., Pott-Pollenske, M., Herr, M., and Delfs, J., "Research at DLR towards airframe noise prediction and reduction," *Aerospace Science and Technology*, Vol. 12, No. 1, 2008, pp. 80–90. https://doi.org/10.1016/j.ast.2007.10.014.